RSC Advances

PAPER

View Article Online
View Journal | View Issue

Cite this: *RSC Adv.*, 2024, **14**, 26123

Photocatalysis oxidative desulfurization of dibenzothiophene in extremely deep liquid fuels on the Z-scheme catalyst ZnO–$CuInS_2$–ZnS intelligently integrated with carbon quantum dots: performance, mechanism, and stability†

Manh B. Nguyen

In this study, we improved the electrochemical and photocatalytic properties of the ZnO–$CuInS_2$–ZnS (ZCZ) material by integrating with carbon quantum dots (CQD) with particle sizes from 2 to 5 nm. The integration of ZnO–$CuInS_2$–ZnS with carbon quantum dots (ZnO–$CuInS_2$–ZnS/CQD:ZCZ–CQD) enhanced the visible light absorption, significantly reduced the electron–hole recombination rate, and facilitated the electron transfer and separation processes as confirmed by UV-visible diffuse reflectance spectroscopy (UV-vis DRS), photoluminescence (PL), and electrochemical impedance spectroscopy (EIS). The successful integration of ZCZ with carbon quantum dots was confirmed using X-ray photoelectron spectroscopy (XPS), energy dispersive spectroscopy (EDS) and transmission electron microscopy (TEM) methods. The ZCZ/CQD photocatalyst removed up to 98.32% of DBT after 120 minutes of reaction, maintained over 90% durability after 10 cycles, and retained its structure without any changes. The ZCZ photocatalyst integrated with CQD enhances faster dibenzothiophene (DBT) removal by 4.46, 3.24, 2.53, and 1.72 times compared to ZnO, $CuInS_2$, ZnS, and ZnO–$CuInS_2$–ZnS, respectively. Factors influencing the oxidation process of DBT including the mass of the photocatalyst, initial DBT concentration, stability, and reaction kinetics were studied. Through active species trapping experiments, this study demonstrated that the formation of $^{\bullet}O_2^-$ and $^{\bullet}OH$ radicals determines the reaction rate. The mechanism of photocatalysis on ZCZ–CQD materials and the intermediate products formed in the process of photocatalytic oxidative desulfurization of dibenzothiophene is proposed based on electrochemical measurements and GC-MS results.

Received 24th June 2024
Accepted 6th August 2024

DOI: 10.1039/d4ra04599h

rsc.li/rsc-advances

1 Introduction

Sulfur compounds in fuels have a negative impact on the environment, being the main cause of SO_x emissions in air and acid rain.[1] Therefore, policies and regulations on sulfur content in fuels are increasingly strict worldwide. Methods for the removal of sulfur compounds in liquid fuels include hydroprocessing, oxidation, adsorption, and hydrodesulfurization.[2–4] Hydrodesulfurization (HDS) is a traditional method performed at a high temperature and pressure (320–380 °C, 3–7 MPa) using a large amount of hydrogen for the hydrogenation, leading to an inefficient removal of sulfur compounds.[5] Furthermore, sulfur compounds such as alkylthiophenes, dibenzothiophene (DBT), benzothiophene (BT), dibenzothiophene (DBT) and 4,6-dimethyldibenzothiophene (4,6-DMDBT) are very difficult to remove using HDS technology.[6,7] To overcome the drawbacks of removing sulfur compounds at high temperatures and pressures, requiring large amounts of hydrogen, and the inability to remove sulfur compounds with stable structures such as BT, 4,6-DMDBT and DBT, oxidative desulfurization and photocatalytic oxidative desulfurization (PODS) methods have been developed to remove sulfur compounds at ambient temperature and atmospheric pressure using energy-saving, low cost, non-toxic, and easy operation, and especially for the deep removal of sulfur-containing compounds.[8]

ZnO and ZnS materials are considered to be highly efficient photocatalysts owing to their low cost, non-toxic nature, and stable photocatalytic properties.[9–11] However, they have some drawbacks that need to be addressed, such as high bandgap energy, absorption of ultraviolet light, and rapid recombination rate between electrons and holes.[12] Recently, ZnO and ZnS have been modified with polymers, metal oxides, and g-C_3N_4 to enhance their visible light absorption capability and reduce the

Institute of Chemistry, Vietnam Academy of Science and Technology, 18 Hoang Quoc Viet, Cau Giay, Hanoi, Vietnam. E-mail: nguyenbamanh@ich.vast.vn

† Electronic supplementary information (ESI) available: XPS spectra and Mott–Schottky (MS) plot of ZnS, $CuInS_2$ and ZnO samples. SEM image of ZCZ–CQD sample. GC-MS spectra of the products in the desulfurization of DBT over ZnO–$CuInS_2$–ZnS/CQD photocatalyst. See DOI: https://doi.org/10.1039/d4ra04599h

electron–hole recombination rate. Lifshagerd *et al.*[13] enhanced the visible light absorption capability of ZnO by modifying it with nanoparticles of CeO_2 and $CeFeO_3$, which are active catalysts that have a faster tetracycline degradation rate that is 2.12 times faster than that of ZnO and maintain high tetracycline degradation efficiency for at least four reaction cycles. Borthakur *et al.*[14] successfully synthesized a ZnO@g-C_3N_4 nanocomposite with an N-doped phase that exhibited 2.5 and 5 times higher degradation efficiency towards crystal violet (CV) compared to g-C_3N_4 and N-doped ZnO, respectively. Kai *et al.*[15] modified ZnO with CdS and ZnS to produce a stable hydrogen evolution catalyst that maintained activity for at least 72 hours with a hydrogen production rate of 2.64 mmol g^{-1} h^{-1}, higher than pure ZnO catalyst (0.33 mmol g^{-1} h^{-1}). Cui *et al.*[11] developed a heterojunction catalyst $CuInS_2$/ZnS for rapid degradation of tetracycline under visible light, achieving an efficiency of 86% after 3 hours of reaction.

Recently, $CuInS_2$ material has been utilized as an efficient photocatalyst for environmental treatment due to its low band gap energy (<1.5 eV), visible light absorption, and low toxicity.[16] However, $CuInS_2$ suffers from poor chemical stability, low surface area, and aggregation during reactions, leading to poor charge separation and transfer.[17] Qiao *et al.*[18] enhanced the hydro production efficiency to 4188.25 μmol g^{-1}, which is 623.7 times higher than $CuInS_2$ by synthesizing ZnO/$CuInS_2$ photocatalysts. Thus, different semiconductors are combined together, creating semiconductors with many advantages such as (i) wider light absorption range compared to individual semiconductors, (ii) reduced recombination rate of electron–hole pairs, and (iii) more efficient charge transport and separation processes.[11,17] However, although different semiconductors are combined, the contact between them is poor, leading to the slow movement of electrons between the active phases.[19–21] Therefore, increasing the contact between semiconductor materials facilitates the diffusion, transport, and movement of charges and electrons more effectively, transferring charges faster to enhance the efficiency of photocatalysis. Recently, some authors have reported the combination of metal–organic frameworks (MOFs) and carbon quantum dots (CQD) to enhance the efficiency of photocatalysis by accelerating the charge transfer process, reducing charge recombination, and increasing effective light absorption.[22–24] Furthermore, CQDs have many other advantages, such as being inexpensive, abundant, small in size, high electrical conductivity, biocompatible, low toxicity, fluorescent, high optical intensity, and broad light absorption range.[25–27]

In this study, a third-order ZnS–$CuInS_2$–ZnS photocatalyst was rapidly integrated with carbon quantum dots (CQDs) using a microwave-assisted method. The ZnO–$CuInS_2$–ZnS/CQD photocatalyst was applied for DBT oxidation in a model fuel sample. Factors affecting the DBT oxidation process, including the catalyst mass, initial DBT concentration, O/S ratio, stability, and reaction kinetics, have been studied. The mechanism of photocatalysis on ZCZ–CQD materials and the intermediate products formed in the process of photocatalytic desulfurization oxidative of dibenzothiophene has been proposed based on electrochemical measurements and GC-MS results.

2 Experimental methods

2.1 Synthesis of carbon quantum dots (CQD)

Carbon quantum dots are synthesized by a hydrothermal method from a chitosan source, as reported in our previous study.[28] Specifically, chitosan with a concentration of 5 g L^{-1} in a 1% CH_3COOH solution is heated at 180 °C for 12 h. The resulting mixture is then separated to remove solid impurities and obtain a yellowish solution (CQD).

2.2 Synthesis of ZnO material

ZnO material is synthesized using a green method using orange peel extract.[29] Specifically, the orange peel is cleaned, dried, and ground into fine powder. Next, 2 g of the orange peel powder is added to 100 mL of distilled water and stirred for 3 hours, and then the mixture is heated to 60 °C for 60 minutes. The solid material is then separated to obtain the orange peel extract solution used to synthesize ZnO. Then, 4 g of $Zn(NO_3)_2 \cdot 2H_2O$ was added to 95 mL of the orange peel extract solution. Next, this mixture is heated at 60 °C for 60 minutes and vigorously stirred. Then, the mixture is dried at 150 °C and heat-treated at 400 °C for 1 hour to obtain a white ZnO material.

2.3 Synthesis of $CuInS_2$ material

$CuInS_2$ material is synthesized by a solvothermal method using the following steps: specifically, 10 mmol of $CH_3(CH_2)_{11}OSO_3Na$ (2.884) is dissolved in 50 mL of ethylene glycol (EG, 98%) and stirred for 15 minutes at 70 °C (solution A). At the same time, 2 mmol of $InCl_3$ (0.586 g), 2 mmol of $Cu(NO_3)_2$ (0.483 g) and 5 mmol of thioacetamide (C_2H_5NS, 0.375 g) are dissolved in 20 mL of water and vigorously stirred for 30 minutes at 70 °C (solution B). Next, solution B is slowly added to solution A, and this mixture is then transferred to a Teflon flask and hydrothermally treated with microwave assistance at 100 °C for 30 minutes to obtain a black colloidal mixture. The solid is separated by centrifugation, washed several times with distilled water and ethanol, and dried at 80 °C for 12 hours to obtain the black $CuInS_2$ material.

2.4 Synthesis of ZnS material

4 mmol of $Zn(NO_3)_2 \cdot 6H_2O$ and 5 mmol of thioacetamide are dissolved in 20 mL of distilled water and vigorously stirred to create a homogeneous solution. Next, this mixture is added to 50 mL of ethylene glycol (EG, 98%) and placed in a Teflon and water bath with microwave assistance at 100 °C for 30 minutes to obtain a white fluffy mixture. The solid is separated by centrifugation, washed several times with distilled water and ethanol, and dried at 80 °C for 12 hours to obtain the white ZnS material.

2.5 Synthesis of ZnO–$CuInS_2$–ZnS/CQD materials

The ZnO–$CuInS_2$–ZnS/CQD material with the mass ratio of the components is synthesized according to our previous report. Specifically, 0.3 g of $CuInS_2$, 0.2 g of ZnO, and 0.5 g of ZnS were added to 50 mL of C_2H_5OH and dispersed evenly by

ultrasonication for 1 hour (mixture A). At the same time, 10 mL of the CQD synthesized above was dispersed in 50 mL of a mixture of ethanol and water (volume ratio 1 : 4) (solution B). Next, slowly add solution A to solution B, sonicate for 0.5 hours, and transfer to a Teflon vial for microwave hydrothermal treatment at 120 °C for 30 minutes. The mixture is allowed to cool naturally to room temperature and the solid is separated by centrifugation and washed with pure water. Finally, the solid is dried at 70 °C for 12 hours to obtain the ZnO–$CuInS_2$–ZnS/CQD material.

2.6 Photocatalytic oxidative desulfurization

Preparation of the model fuel: 300 mg of dibenzothiophene (DBT) is dissolved in 1000 mL of *n*-octane solvent. Then, 0.1 g of photocatalyst is added to 100 mL of DBT solution (300 mg L^{-1}) and stirred in the dark for 60 minutes to achieve the adsorption–desorption equilibrium. Next, 0.75 mL L^{-1} of H_2O_2 is added to the reaction mixture, and a 300 W xenon lamp with a light intensity of about 6160 lux is used to activate the photocatalyst. After 20 minutes, 2 mL of the reaction solution is extracted and the catalyst is separated to analyze the concentration of DBT at time *t*. Using a circulating water bath to maintain the temperature in the continuous reaction system at 25 °C. The removal of DBT in the model oil was evaluated by analyzing the DBT concentration in the *n*-octane before and after reaction using UV-vis spectroscopy at a wavelength of λ_{max} = 325 nm.[30–32] The efficiency of DBT removal at time *t* is calculated by formula (1):

$$H = \frac{C_o - C_t}{C_o} \times 100 \quad (1)$$

where % *H*, C_t and C_o are the DBT removal efficiency, DBT concentration at time *t* and initial DBT concentration, respectively.

To study the influencing factors, different values of DBT concentration (200 to 500 mg L^{-1}), ZCZ–CQD photocatalyst dosage (0.5, 1.0, 1.5, and 2.0 g L^{-1}), and H_2O_2 amount (0.25, 0.5, 0.75, 1.0 and 1.25 mL L^{-1}) were investigated.

3 Result and discussion

3.1 Characterization of ZnO, ZnS, $CuInS_2$ and ZCZ–CQD samples

The phase structures of ZnO, ZnS, $CuInS_2$, and ZnO–$CuInS_2$–ZnS–CQD (ZCZ–CQD) samples have been determined using the X-ray diffraction (XRD) method and presented in Fig. 1. The XRD pattern of the ZnO sample shows diffraction peaks at 2θ of 31.95° (110), 34.52° (002), 36.41° (101), and 47.74° (102), which are characteristic of the wurtzite phase of ZnO (JCPDS No. 36-1451).[33–35] The diffraction peaks at 2θ of 27.63° (100), 28.91° (002), 29.38° (101) and 48.01° (110) are characteristic of the chalcopyrite phase of $CuInS_2$ (JCPDS No. 85-1575).[36,37] The XRD pattern of the ZnS sample shows diffraction peaks at 2θ of 28.48° and 45.52°, which are characteristic of the (111) and (220) reflection planes of sphalerite ZnS (PDF # 05-0566).[38–40] For the ZnO–$CuInS_2$–ZnS/CQD sample, all characteristic peaks of

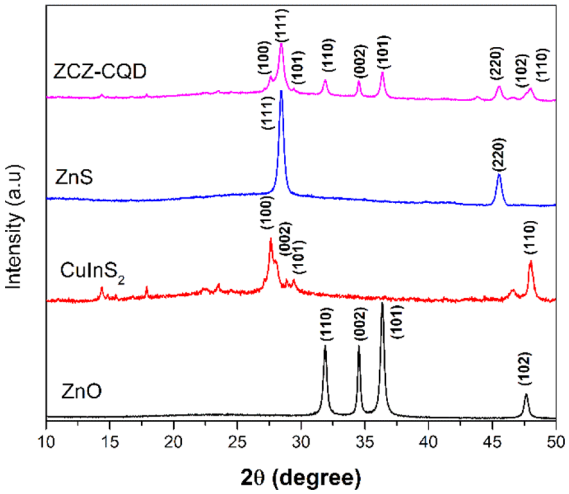

Fig. 1 XRD patterns of ZnO, ZnS, $CuInS_2$ and ZCZ–CQD samples.

$CuInS_2$, ZnS, and ZnO phases were fully present, indicating the successful synthesis of the ZnO–$CuInS_2$–ZnS/CQD composite. However, no characteristic peaks of CQD were observed, which may be due to the low content of CQD and the amorphous structure of CQD.[28] The crystal grain sizes of ZnO, $CuInS_2$, and ZnS samples were determined by the Debye–Scherrer equation to be 14.2, 16.0, and 15.6 nm, respectively.

The chemical composition of ZnO, $CuInS_2$, ZnS and ZCZ–CQD materials was determined by the energy-dispersive X-ray spectroscopy (EDS) method. EDS mapping images and EDS analysis of the ZCZ–CQD material in Fig. 2 show the presence of elements Zn, Cu, In, S, O, C, and N. As stated in Table S1,† the elemental composition of Zn, O, Cu, In, S, C, and N in the ZCZ–CQD material are 47.28, 6.38, 6.29, 14.24, 22.16, 2.7, and 0.95% wt, respectively.

The X-ray photoelectron spectroscopy (XPS) method is used to determine the elemental composition and oxidation state of

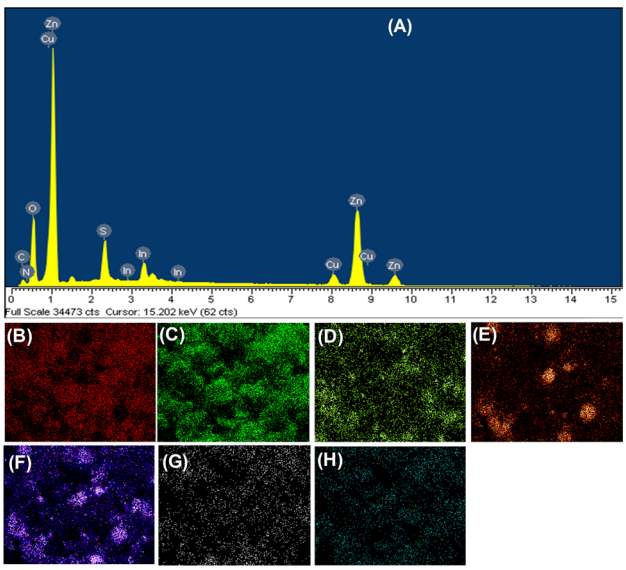

Fig. 2 EDS spectrum (A), EDS element mapping images of Zn (B), O (C), Cu (D), In (E), S (F), C (G) and N (H) of the ZCZ–CQD sample.

the surface of $CuInS_2$, ZnO, ZnS, and ZCZ–CQD materials (Fig. 3). The C 1s peak at a binding energy of 284.8 eV is used to calibrate the binding energy of $CuInS_2$, ZnO, ZnS, and ZCZ–CQD materials.[41] As shown in Fig. S2,† the full-scan XPS spectra confirm the presence of Zn 2p (1022 and 1045 eV), Cu 2p (932 and 952 eV), In 3d (445 and 453 eV), O 1s (531 eV), S 2p (161 eV), and C 1s (284 eV) in the ZCZ–CQD sample.[42–44] In the ZnO sample, the high-resolution Zn 2p XPS spectra have two peaks at binding energies of 1021.57 eV (Zn $2p_{3/2}$) and 1044.66 eV (Zn $2p_{1/2}$) assigned to Zn^{2+}.[45] Meanwhile, the high-resolution O 1s XPS spectrum is split into two peaks at binding energies of 531.22 and 532.77 eV assigned to O_2^- in the (Zn–O) lattice and the –OH groups.[46] For the $CuInS_2$ sample, peaks are observed at binding energies of Cu^+ (932.04 and 951.81 eV), Cu^{2+} (933.17 and 953.19 eV), In^{2+} (444.95 and 452.58 eV) and In^{3+} (445.74 and 453.12 eV).[47] The high-resolution S 2p XPS spectra peaks at binding energies of 161.59 and 163.26 eV are assigned to S $2p_{3/2}$ and S $2p_{1/2}$, consistent with the presence of the S^{2-} state in both ZnS and $CuInS_2$ samples. The high-resolution Zn 2p XPS spectra of the ZnS sample show peaks at 1021.64 eV and 1044.77 eV assigned to Zn $2p_{3/2}$ and Zn $2p_{1/2}$.[45] For the ZCZ–CQD sample, the presence of Zn^{2+} (1021.86 and 1044.77 eV), Cu^+ (931.56 and 951.50 eV), Cu^{2+} (932.85 and 952.93 eV), In^{2+} (444.63 and 452.22 eV), In^{3+} (445.37 and 452.86 eV) and S^{2-} (161.54 and 163.16 eV) are noted. The high-resolution O 1s XPS spectra of the ZCS–CQD sample reveals three peaks at binding energies of 530.22; 531.57 and 532.36 eV assigned to C–O/C=O, O^{2-} (Zn–O) in the lattice and the –OH groups, respectively.[48]

Furthermore, the high-resolution C 1s XPS spectra is separated into three peaks at binding energies of 284.77 eV (C–C/C=C), 286.31 eV (C–O), and 288.40 eV (C=O).[48,49] The presence of characteristic C=O, C–C, C=C, and C–O bonds has demonstrated the formation of bonds between CQD and the ZnO–$CuInS_2$–ZnS composite. The XPS results clearly indicate the simultaneous presence of $CuInS_2$, ZnS, ZnO, and CQD, which is consistent with XRD and EDS-mapping results. Additionally, the binding energy peaks of Zn 2p and O 1s in the ZCZ–CQD sample are shifted to higher binding energies compared to the ZnO and ZnS samples. Conversely, the binding energies of Cu 2p, In 3d, and S 2p receive additional electrons, causing a shift in binding energy towards the negative direction.[50]

From the results of electronic transport measurements, the electron transport pathway of the semiconductor ZCZ–CQD can be determined as follows: electrons in ZnO and ZnS move to the interface between the semiconductors before moving through the semiconductor $CuInS_2$ *via* the CQD bridge. This energy change indicates strong surface interactions between these elements in the heterostructure.[51] Therefore, the CQD bridge helps enhance the tight binding of the semiconductors, facilitating the electron transport process within the material.

The N_2 adsorption–desorption isotherms of $CuInS_2$, ZnO, ZnS, and ZCZ–CQD materials have been analyzed at 77 K. The ZnO, $CuInS_2$, ZnS, and ZCZ–CQD materials have N_2 adsorption–desorption isotherms classified as type IV according to the IUPAC classification (Fig. 4).[52] Among these materials, $CuInS_2$

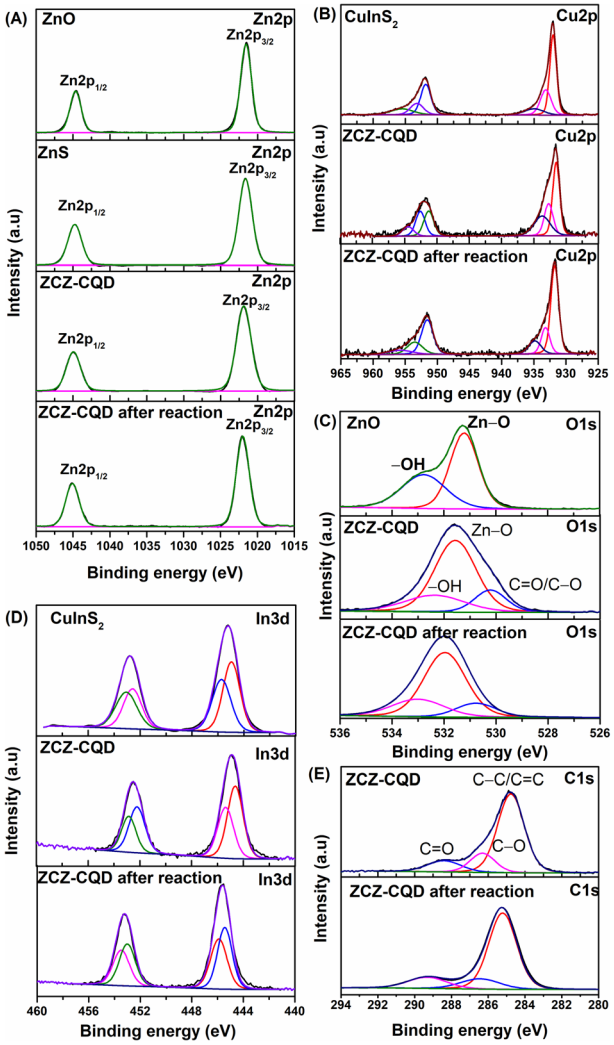

Fig. 3 High-resolution Zn 2p (A), Cu 2p (B), O 1s (C), In 3d (D) and C 1s (E) XPS spectra of ZnO, $CuInS_2$, ZnS and ZCZ–CQD and CZC–CQD after 10 cycles.

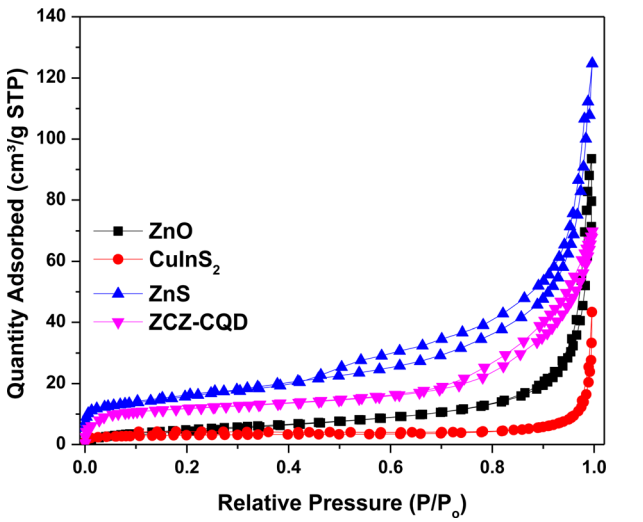

Fig. 4 N_2 adsorption–desorption isotherms of $CuInS_2$, ZnO, ZnS, and ZCZ–CQD samples.

has the lowest specific surface area (10.88 $m^2\ g^{-1}$) and pore volume (0.038 $cm^3\ g^{-1}$). On the other hand, ZnS has the largest specific surface area (54.94 $m^2\ g^{-1}$) and pore volume (0.196 $cm^3\ g^{-1}$). The specific surface area and pore volume of ZCZ–CQD are 36.39 $m^2\ g^{-1}$ and 0.138 $cm^3\ g^{-1}$, respectively. The average pore diameter of ZnO, $CuInS_2$, ZnS, and ZCZ–CQD materials are 14.99, 13.78, 15.07, and 14.26 nm, respectively (Table 1). It can be seen that larger pore diameters of materials are advantageous for the diffusion process of reactants to active sites, thereby enhancing the efficiency of DBT removal in fuels.

The morphology of ZnO, ZnS, $CuInS_2$, and ZCZ–CQD materials was determined by transmission electron microscopy (TEM) and presented in Fig. 5. TEM images of the ZnO sample show the particles are spherical in shape, with nanoparticle sizes of 20–30 nm and relatively uniform. $CuInS_2$ material appears as flower-like structures with non-uniform sizes.[53] TEM images of the ZnS material show a tendency to aggregate into spherical particles with particle sizes of 20–50 nm, consistent with the report by Boulkroune *et al.*[54] The TEM images of the ZCZ–CQD material reveal nano-sized ZnO and ZnS particles with sizes around 20–30 nm and a fairly even distribution. The TEM images show close contact between ZnO, $CuInS_2$, and ZnS nanoparticles, forming a heterostructure. However, the flower-like structures of $CuInS_2$ are difficult to observe in TEM images but can be easily seen in SEM images (Fig. S4†). Therefore, TEM and SEM images confirm the successful integration of the ZnO–$CuInS_2$–ZnS material with carbon quantum dots of ultra-small particle sizes of 1–2 nm using a microwave-assisted hydrothermal method.

The photoelectrochemical properties, including UV-visible diffuse reflectance spectra (UV-vis DRS), photoluminescence (PL), Mott–Schottky and electrochemical impedance spectroscopy (EIS) of $CuInS_2$, ZnO, ZnS, and ZSZ–CQD samples are presented in Fig. 6. ZnS and ZnO materials have a strong ability to absorb ultraviolet light, and bandgap energies are 3.52 and 3.2 eV, respectively.[55] On the other hand, $CuInS_2$ absorbs visible light, and the bandgap energy is 1.17 eV. The combination of ZnO–$CuInS_2$–ZnS and ZnO–$CuInS_2$–ZnS/CQD has shifted the light absorption energy from ultraviolet to visible light. The interaction between ZnO, $CuInS_2$, and ZnS phases through CQD has increased the light absorption capability and reduced the bandgap energy of the ZnO–$CuInS_2$–ZnS material when integrating CQD. Furthermore, the ability to absorb light in the visible range of 500–800 nm is enhanced after combining CQD with a third-order ZCZ catalyst. This has promoted the electron transfer process and enhanced the ability to absorb light in the visible range.[56] The flat band potentials (E_{fb}) of ZnO, $CuInS_2$,

Table 1 BET parameters and E_g of $CuInS_2$, ZnO, ZnS and ZCZ–CQD samples

Samples	S_{BET} ($m^2\ g^{-1}$)	V_{pore} ($cm^3\ g^{-1}$)	D_{BJH} (nm)	E_g (eV)
ZnO	19.12	0.100	14.99	3.20
$CuInS_2$	10.88	0.038	13.78	1.17
ZnS	54.94	0.196	15.07	3.52
ZCZ–CQD	36.39	0.138	14.26	2.76

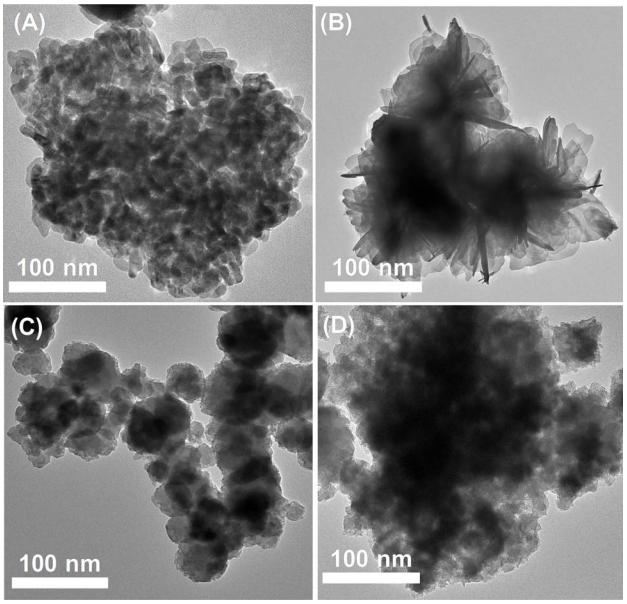

Fig. 5 TEM images of ZnO (A), $CuInS_2$ (B), ZnS (C) and ZCZ–CQD (D) samples.

and ZnS materials were determined using the Mott–Schottky method, as presented in Fig. S5.† The flat band potentials (E_{fb}) of ZnO, $CuInS_2$, and ZnS samples determined using the Mott–Schottky method are −1.08, −1.56, and −1.20 eV, respectively. The E_{fb} values using a standard normal hydrogen electrode (NHE) can be determined according to eqn (2), and $E_{(NHE)}$ for ZnO, $CuInS_2$, and ZnS are −0.47, −0.95, and −0.59 eV, respectively.

$$E_{(NHE)} = E_{Ag/AgCl} + 0.059pH + E^{\circ}_{Ag/AgCl} \quad (2)$$

$E^{\circ}_{Ag/AgCl} = 0.1976$ V and $E_{Ag/AgCl}$ is the activity potential of Ag/AgCl at pH = 7.

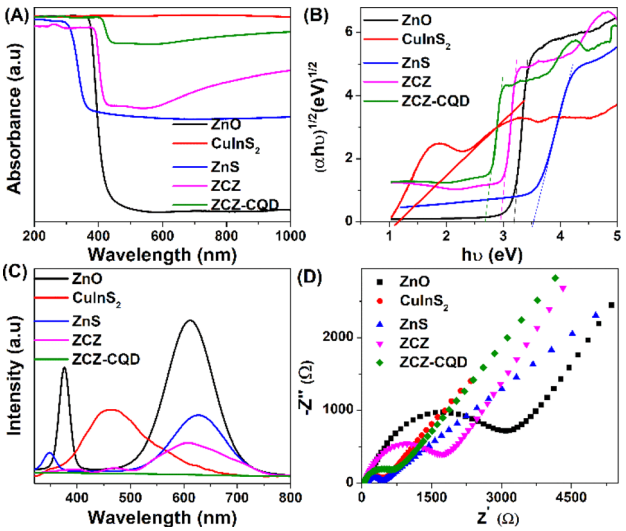

Fig. 6 UV-vis DRS spectrum (A), bandgap energy (E_g) (B), photoluminescence spectra (C), EIS spectra (D) of ZnO, $CuInS_2$, ZnS, ZCZ and ZCZ–CQD samples.

The valence band energy (E_{VB}) difference compared to NHE is approximately 0.2 or 0.1 eV for n-type semiconductors, so we consider it to be 0.1 eV. The CB values of ZnO, $CuInS_2$, and ZnS materials are −0.57, −1.05, and −0.69 eV, respectively. Based on the relationship between the E_g and the conduction band edge (E_{CB}), the valence band energy (E_{VB}) can be calculated using eqn (3):

$$E_{VB} = E_g + E_{CB} \quad (3)$$

The VB potentials of ZnO, $CuInS_2$, and ZnS materials are 2.63, 0.12, and 2.83 eV, respectively.

The photoluminescence (PL) is characteristic of the recombination speed of charged particles between the hole and the electron. Fig. 6C shows that the ZnO material has the highest photoluminescence intensity, with emission wavelengths ranging from 350–400 nm and 500–700 nm, indicating a rapid recombination speed between electrons and holes. When combining the semiconductors ZnO, ZnS, and $CuInS_2$ together, the peak intensity is significantly reduced due to the combination of different semiconductors causing electrons to shift from one phase to another through the CQD bridge, leading to a significant decrease in electron–hole recombination.[26] The photoluminescence intensity of the materials is in the order ZnO > $CuInS_2$ > ZnS > ZCZ > ZCZ–CQD. The ZCZ sample modified with CQD has the lowest PL intensity due to low recombination and effective charge separation. The movement of photo-generated electrons from the CB of ZnO and ZnS to the VB of $CuInS_2$ increases the separation, leading to a decrease in emission and recombination ability in the semiconductor. Additionally, CQD helps transfer double Z and reduce electron–hole recombination.[26]

The charge transfer rate of ZnO, $CuInS_2$, ZnS, ZCZ, and ZCZ–CQD materials has been determined through the electrochemical impedance spectroscopy (EIS) method. The charge transfer resistance values (R_{ct}) of ZnO, $CuInS_2$, ZnS, ZCZ, and ZCZ–CQD materials are 3180, 412, 461, 1692, and 734 Ω, respectively. The results show that $CuInS_2$ and ZnS materials have the best charge transfer capability, with the smallest semicircle in the Nyquist plot. In contrast, ZnO shows slow charge transfer capability with a large semicircle. When $CuInS_2$ and ZnS are combined with ZnO, the semicircle diameter of the ZCZ composite material decreases significantly, demonstrating a change in optoelectronic properties due to the formation of interfacial bonds through CQD bridges. The ZCZ–CQD material has a smaller semicircle diameter compared to the ZCZ sample, confirming that modifying ZCZ with CQD benefits the charge transport process. The formation of interfacial bonds through CQD is also confirmed by the EIS results, as the semicircle of the ZCZ sample with added CQD is much smaller than the ZCZ–CQD sample without CQD.

3.2 Photocatalytic activity

ZnO, ZnS, $CuInS_2$, and ZnO–$CuInS_2$–ZnS/CQD materials were used to evaluate the dibenzothiophene removal process by photocatalysis (Fig. 7A). ZnO, ZnS, and $CuInS_2$ materials removed DBT after 120 minutes with efficiencies of 45.29%, 67.18%, and 57.83%, respectively, under visible light irradiation. The low DBT removal efficiency of ZnO and $CuInS_2$ samples is due to their low surface area and fast recombination rate between electrons and holes, leading to a low rate and quantity of reactive species formation ($^{\bullet}O_2^-$ and $^{\bullet}OH$). Additionally, ZnO and ZnS absorb UV light, resulting in low DBT removal efficiency. Interestingly, ZnO–$CuInS_2$–ZnS (81.62%) and ZnO–$CuInS_2$–ZnS/CQD (94.63%) samples showed higher DBT removal efficiency compared to individual ZnO, $CuInS_2$, and ZnS samples. This may be due to (i) the reduced recombination rate of the photo-generated electron–hole pairs, (ii) enhanced visible light absorption capability, and (iii) synergistic effect of phase activities. The ZnO–$CuInS_2$–ZnS/CQD sample has a faster DBT removal rate compared to the ZnO–$CuInS_2$–ZnS sample due to its faster electrical conductivity, generating more reaction radicals. This result is explained by the CQD facilitating the movement of charged particles by creating bonds between the reactive phases.[28] The first-order pseudo rate constants for the DBT removal process on the ZnO, $CuInS_2$, ZnS, ZCZ, and ZCZ–CQD photocatalysts are 0.0056, 0.0077, 0.0099, 0.0145, and 0.0250 min^{-1}, respectively (Fig. 7B). Therefore, the DBT removal rates of the ZCZ–CQD photocatalysts are 4.46, 3.24, 2.53, and 1.72 times faster than the ZnO, $CuInS_2$, ZnS, and ZCZ photocatalysts.

The ZnO–$CuInS_2$–ZnS/CQD photocatalyst is used to investigate the factors affecting the DBT removal process, including the initial DBT concentration, catalyst dosage, and O/S ratio.

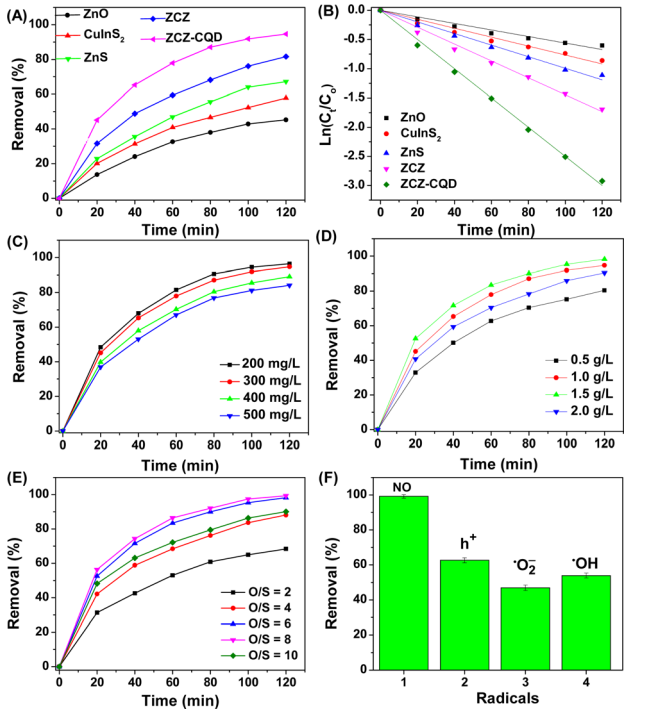

Fig. 7 (A) Removal efficiency of DBT, (B) pseudo-first-order kinetic models of ZnO, $CuInS_2$, ZnS, ZCZ and ZCZ–CQD photocatalysts; removal efficiency of DBT over ZCZ–CQD photocatalyst at different DBT concentrations (C), catalysts dose (D), O/S molar ratio (E), reactive radicals (F).

Fig. 7C confirms that as the initial DBT concentration decreases, the DBT removal efficiency increases. Specifically, the DBT removal efficiency on the ZCZ/CQD photocatalyst reaches 96.38% after 120 minutes of visible light irradiation, with an initial DBT concentration of 200 mg L^{-1}. When the DBT concentration increases to 500 mg L^{-1}, the DBT removal efficiency decreases from 96.38% to 84.08% after 120 minutes of reaction. At initial DBT concentrations of 300 mg L^{-1} (94.63%) and 200 mg L^{-1} (96.38%), the DBT removal efficiency does not change significantly, so we choose a DBT concentration of 300 mg L^{-1} to investigate other factors such as catalyst dosage and H_2O_2 concentration. Fig. 7D confirms that the removal efficiency of DBT decreased from 98.19% to 80.38% when the ZCZ–CQD photocatalyst dosage decreased from 1.5 to 0.5 g L^{-1}. A decrease in catalyst dosage implies a reduction in active sites, resulting in a decrease in DBT removal efficiency. It can be seen that for a catalyst dosage of 2 g L^{-1}, the DBT removal efficiency decreased compared to using a dosage of 1.5 g L^{-1}. When using an excessive catalyst dosage, the catalyst becomes too dispersed in the solution, leading to a decrease in the visible light absorption capacity of the catalyst, consistent with previous reports by Nui *et al.*[57]

Fig. 7E confirms that the O/S mol ratio affects the efficiency of DBT removal. Specifically, the DBT removal efficiency increases from 68.64% to 98.32% when the O/S mol ratio increases from 2 to 8. When the O/S ratio exceeds the optimal level, going from 8 to 10, the DBT removal efficiency decreases from 98.32% to 88.11%. This result may be due to the excessive increase in the number of ˙OH groups, creating favorable conditions for the formation of ˙OOH radicals, which may DBR removal less effectively than the ˙OH radical. Therefore, the optimal conditions are determined on the ZnO–$CuInS_2$–ZnS/CQD catalyst as a catalyst dosage of 1.5 g L^{-1}, DBT concentration of 300 mg L^{-1}, and O/S mol ratio of 8.

The intermediate product of the DBT sulfur removal process on the catalyst was analyzed by GC-MS (Fig. S6†). In Fig. S6A,† the ion signal at a retention time of 20.62 corresponds to the initial DBT. After increasing the irradiation time, the signal intensity at a retention time of 20.62 decreases, and the signal intensity at a retention time of 24.22 assigned to DBT–O_2 increases. Thus, the GC-MS results have confirmed that the main product of the DBT sulfur removal process on the ZCZ–CQD photocatalyst is DBT–O_2. The DBT removal efficiency of the ZCZ–CQD photocatalyst was compared with other photocatalysts (Table S3†), showing that our ZCZ–CQD sample outperforms previously reported photocatalysts in terms of DBT removal efficiency.

3.3 Mechanism discussion

Photo-generated holes (h^+) and reactive radicals (˙OH, $\cdot O_2^-$) act as oxidizing agents to convert DBT to DBT–O_2. To determine the roles of the reactive radicals and the reaction mechanism, we used radical scavengers and hole traps, including *p*-benzoquinone (*p*-BQ, $\cdot O_2^-$), disodium ethylenediaminetetraacetate (Na_2–EDTA, h^+), and *tert*-butyl alcohol (TBA, ˙OH). In Fig. 8A, the radical scavengers and hole traps, including TBA, Na_2–EDTA, and *p*-BQ, significantly reduced the efficiency of DBT removal,

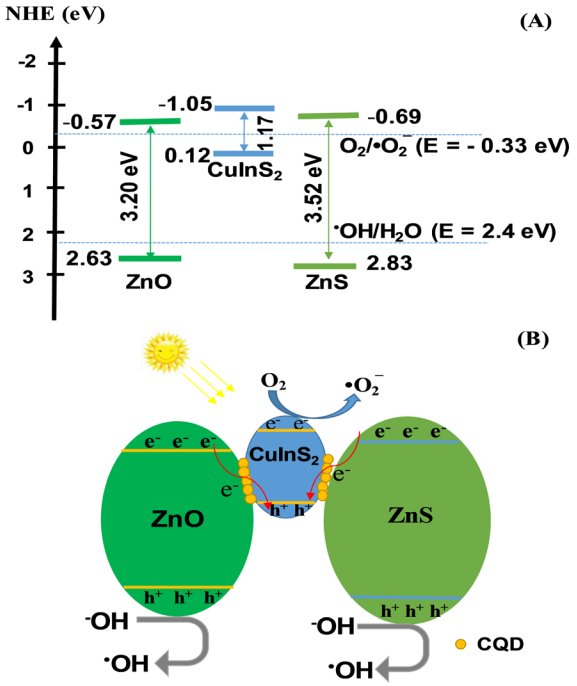

Fig. 8 Mechanism diagram of the charge transfer before contact (A) and possible Z-scheme (B) of ZnO, $CuInS_2$, ZnS, and ZCZ–CQD.

confirming that the $\cdot O_2^-$, ˙OH radicals, and photo-generated holes (h^+) all participate in the oxidation process of DBT to DBT–O_2.

We construct the band structure of materials based on the optoelectronic and electrochemical properties of ZnO, $CuInS_2$, and ZnS. Fig. 8A shows that the conduction band energy (CB) of ZnS, $CuInS_2$, and ZnO are all more negative than the standard oxidation potential $E°(O_2/\cdot O_2^-$, −0.33 eV), so the electrons on the CB can react with O_2 adsorbed on the material surface to form $\cdot O_2^-$ radicals.[42] At the valence band (VB), the conduction band energy of ZnO and ZnS is higher than that of ˙OH/H_2O (2.4 eV), so the photo-generated holes can combine with H_2O or OH^- groups to form reactive ˙OH radicals. However, at the VB of $CuInS_2$, the h^+ of $CuInS_2$ (0.65 eV) has lower energy than that of ˙OH/H_2O (2.4 eV), so h^+ cannot react with OH^- or H_2O to generate ˙OH radicals.[58]

As shown in Fig. 8B, under the influence of light, the ZCZ–CQD (Z-scheme) photocatalyst is excited and separated into electrons and holes. The electrons move to the conduction band (CB) of the semiconductor ZnO, $CuInS_2$, and ZnS (eqn (4)). CQD can absorb visible light and convert it into short-wavelength ultraviolet light to further stimulate the heterojunction material to generate more electrons and holes.[56] The ZCZ–CQD material prevents the recombination process of charges, as the CQD traps the electrons in ZnO, $CuInS_2$, and ZnS, enhancing the charge separation ability. At the conduction band (CB) positions of ZnO, $CuInS_2$, and ZnS, electrons combine with oxygen to form superoxide radicals $\cdot O_2^-$ (eqn (5)). Moreover, electrons in the conduction band of ZnO (−0.57 eV) and ZnS (−0.69 eV) move to $CuInS_2$ and combine with the holes of $CuInS_2$ (eqn (6) and (7)). At the valence band (VB) of ZnO (2.63

eV) and ZnS (2.83 eV), the energy of holes was higher than that of $^{\bullet}OH/H_2O$, so these holes react with water or hydroxyl groups molecules adsorbed on the surfaces to produce high levels of hydroxyl radicals ($^{\bullet}OH$) (eqn (8)).

$$ZnO–CuInS_2–ZnS/CQD + h\nu \rightarrow ZnO–CuInS_2–ZnS/CQD \text{ (holes } (h^+) \text{ and electrons } (e^-)) \quad (4)$$

$$O_2 + (e^-) \rightarrow {}^{\bullet}O_2^- \text{ radicals} \quad (5)$$

$$e^- + H_2O_2 \rightarrow OH^- + {}^{\bullet}OH6$$

$$ZnO(e^-) \text{ and } ZnS(e^-) \rightarrow CQD \rightarrow CuInS_2(e^-) \quad (6)$$

$$ZnO(e^-) + ZnS(e^-) \rightarrow CQD \rightarrow CuInS_2(h^+) \rightarrow CuInS_2(e^- + h^+) \quad (7)$$

$$ZnO(h^+) + ZnS(h^+) + OH^- \text{ or } H_2O \rightarrow {}^{\bullet}OH \quad (8)$$

Finally, the $^{\bullet}O_2^-$, $^{\bullet}OH$ radicals and holes facilitate the conversion of DBT into DBT–O_2 products.

3.4 The stability of ZnO–CuInS$_2$–ZnS/CQD

Stability and reusability play an important role in the application of photocatalysts in reality. Experiments evaluating the stability of the ZCZ–CQD catalyst in the process of DBT removal have been conducted. In Fig. 9, the removal efficiency of DBT reached over 90% after 10 cycles of oxidative desulfurization of DBT after 120 minutes of reaction. This result demonstrates the stability of the ZCZ–CQD catalyst in terms of reusability. The stability of the ZCZ–CQD catalyst has been studied using XRD and XPS methods. The XRD and XPS results showed no significant differences in the phase structure of the ZCZ–CQD material before and after 10 reaction cycles (Fig. 2 and S7†). However, the high-resolution XPS spectra of Zn 2p, O 1s, Cu 2p, In 3d, S 2p, and C 1s confirmed a shift in bond energy to a higher energy region, a result of electrons participating in the reaction with O_2 forming $^{\bullet}O_2^-$ radicals (see Table S2†). Therefore, after 10 reaction cycles of removing DBT, the catalyst still maintains high stability, indicating that the ZCZ–CQD material has a stable structure, tightly bonded together by CQD. In addition, the catalyst Z-scheme catalyst ZCZ–CQD, capable of protecting the high-energy conduction bands, leading to a stable structure of the material.[37]

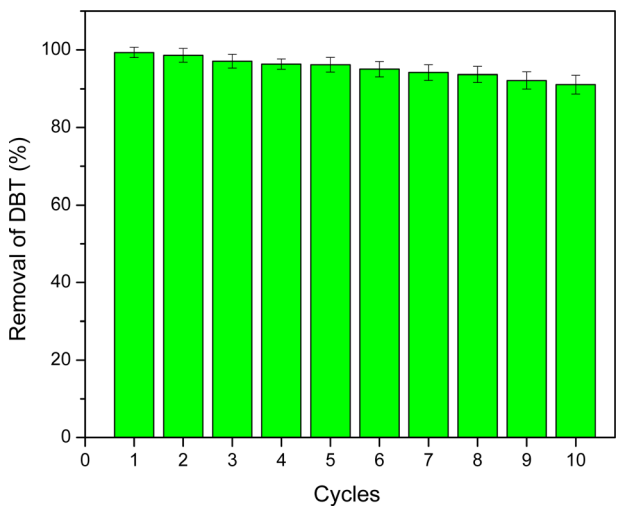

Fig. 9 Stability of photocatalytic activity over ZCZ–CQD at 10 reaction cycles.

4 Conclusion

In this study, the ZnO–CuInS$_2$–ZnS photocatalyst has been successfully integrated with carbon quantum dots using a microwave-assisted hydrothermal method. The carbon quantum dots with a size of 2–5 nm help enhance the absorption of visible light, as well as enhance the electron movement and separation processes in semiconductors through the CQD bridge. The ZnO–CuInS$_2$–ZnS/CQD photocatalyst removed up to 98.32% of DBT after 120 minutes of reaction and achieved over 90% durability after 10 cycles. The ZnO–CuInS$_2$–ZnS photocatalyst integrated with CQD enhances DBT removal faster by 4.46, 3.24, 2.53, and 1.72 times compared to ZnO, CuInS$_2$, ZnS, and ZnO–CuInS$_2$–ZnS, respectively. Factors such as catalyst mass, initial DBT concentration, and O/S molar ratio all significantly affect the DBT removal efficiency. The ZnO–CuInS$_2$–ZnO/CQD catalyst is considered a direct S-type heterojunction catalyst, and the $^{\bullet}O_2^-$ and $^{\bullet}OH$ radicals play an important role in the reaction rate.

Data availability

The author confirms that the data supporting the findings of this study are available within the article.

Author contributions

Manh B. Nguyen: investigation, formal analysis, data curation, writing – original draft, funding acquisition; writing – reviewing and editing; supervision.

Conflicts of interest

There are no conflicts to declare.

Acknowledgements

[Manh B. Nguyen] was funded by the Master, PhD Scholarship Programme of Vingroup Innovation Foundation (VINIF), code [VINIF.2023.TS.066].

References

1 M. B. Nguyen, X. N. Pham and H. V. Doan, *RSC Adv.*, 2021, **11**, 31738–31745.

2 X. Zhang, H. Song, C. Sun, C. Chen, F. Han and X. Li, *Mater. Chem. Phys.*, 2019, **226**, 34–43.
3 X. Zhang, H. Song, C. Sun, C. Chen, F. Han and X. Li, *Mater. Chem. Phys.*, 2019, **226**, 34–43.
4 B. Li, H. Song, F. Han and L. Wei, *Appl. Catal., B*, 2020, **269**, 118845.
5 X. Li, Z. Zhang, C. Yao, X. Lu and X. Zhao, *Appl. Surf. Sci.*, 2016, **364**, 589–596.
6 M. Zarrabi, M. H. Entezari and E. K. Goharshadi, *RSC Adv.*, 2015, **5**, 34652–34662.
7 M. Beshtar, A. Akbar and A. Larimi, *J. Ind. Eng. Chem.*, 2024, **134**, 548–560.
8 M. Ahmad, M. Yousaf, W. Cai and Z. Zhao, *Chem. Eng. J.*, 2023, **453**, 139846.
9 S. Khan, V. Poliukhova and N. Tamir, *Int. J. Hydrogen Energy*, 2022, **48**, 9713–9722.
10 S. Sun, D. Ren, M. Yang, J. Cui and Q. Yang, *Int. J. Hydrogen Energy*, 2021, **47**, 9201–9208.
11 Q. Cui, X. Gu, Y. Zhao, K. Qi and Y. Yan, *J. Taiwan Inst. Chem. Eng.*, 2023, **142**, 104679.
12 A. O. Ali, A. M. E. Naggar, A. S. Morshedy, W. A. Aboutaleb and N. H. Metwally, *Chemosphere*, 2022, **307**, 136011.
13 F. Andish-Lifshagerd, A. Habibi-Yangjeh, M. Habibi and Y. Akinay, *J. Photochem. Photobiol., A*, 2024, **448**, 115351.
14 S. Borthakur, R. Das, P. Basyach and L. Saikia, *RSC Adv.*, 2024, **14**, 1156–1168.
15 K. He, *Int. J. Hydrogen Energy*, 2023, **51**, 30–40.
16 A. Rahman, F. Khan, J. Robert, Y. Kim and M. Mansoob, *Mater. Sci. Semicond. Process.*, 2024, **177**, 108365.
17 J. Zhang, Y. Zhao, K. Qi and S. y. Liu, *J. Mater. Sci. Technol.*, 2024, **172**, 145–155.
18 F. Qiao, W. Liu, J. Yang, Y. Liu and J. Yuan, *Int. J. Hydrogen Energy*, 2024, **53**, 840–847.
19 Y. Wang, J. Chen, X. Yang, X. Liu, M. Que and Y. Ma, *Mater. Today Commun.*, 2023, **37**, 106969.
20 X. Wu, X. Wang, I. Lynch, Z. Guo, P. Zhang, L. Wu, P. Ning and N. Ren, *J. Hazard. Mater.*, 2023, **460**, 132323.
21 X. Wang, H. Jing, C. Yu, Q. Li, H. Sun and Z. Chen, *J. Solid State Chem.*, 2023, **325**, 124165.
22 H. Jiang, Y. Zhong, K. Tian, H. Pang and Y. Hao, *Appl. Surf. Sci.*, 2022, **577**, 151902.
23 D. L. Zhao, H. Jin, Q. Zhao, Y. Xu, L. Shen, H. Lin and T. S. Chung, *J. Membr. Sci.*, 2023, **679**, 121706.
24 J. Zhang, R. Liu, M. Kuang, S. Xie, J. Wang and Z. Ji, *Mater. Lett.*, 2023, **101**, 135004.
25 H. Teymourinia, H. A. Alshamsi, A. Al-nayili, E. Sohouli and M. Gholami, *J. Ind. Eng. Chem.*, 2023, **125**, 259–268.
26 A. Kumar, S. K. Sharma, G. Sharma, M. Naushad and F. J. Stadler, *J. Alloys Compd.*, 2020, **838**, 155692.
27 S. Li, X. Liu, Y. Zheng, J. Ma, S. You and H. Zheng, *Chin. Chem. Lett.*, 2023, 108971.
28 M. B. Nguyen, H. V. Doan, D. Le, H. Tan and T. Dai, *J. Environ. Chem. Eng.*, 2024, **12**, 112965.
29 T. U. D. Thi, T. T. Nguyen, Y. D. Thi, K. H. T. Thi, B. T. Phan and K. N. Pham, *RSC Adv.*, 2020, **10**, 23899–23907.
30 M. Abdollahi, A. Larimi, Z. Jiang, F. Khorasheh and C. Ghotbi, *J. Cleaner Prod.*, 2022, **380**, 134968.
31 X. N. Pham, B. M. Nguyen, H. T. Thi and H. V. Doan, *Adv. Powder Technol.*, 2018, **29**(8), 1827–1837.
32 X. N. Pham, M. B. Nguyen, H. S. Ngo and H. V. Doan, *J. Ind. Eng. Chem.*, 2020, **90**, 358–370.
33 A. Uheida, H. G. Mejía, M. Abdel-Rehim, W. Hamd and J. Dutta, *J. Hazard. Mater.*, 2021, **406**, 124299.
34 G. T. T. Pham, H. T. Vu, T. T. Pham, N. N. Thanh, V. N. Thuy, H. Q. Tran, H. V. Doan and M. B. Nguyen, *RSC Adv.*, 2023, **13**, 12402–12410.
35 P. J. Cao, Q. G. Huang, S. T. Navale, M. Fang, X. K. Liu, Y. X. Zeng, W. J. Liu, F. J. Stadler and Y. M. Lu, *Appl. Surf. Sci.*, 2020, **518**, 146223.
36 J. L. Cholula-Díaz, G. Wagner, D. Friedrich, O. Oeckler and H. Krautscheid, *Dalton Trans.*, 2015, **44**, 14227–14234.
37 M. B. Nguyen, P. T. Lan, N. T. Anh, N. N. Tung, S. Guan, V. P. Ting, T. T. B. Nguyen, H. V. Doan, M. T. Tung and T. D. Lam, *RSC Adv.*, 2023, **13**, 35339–35348.
38 C. J. Chang, Y. H. Wei and K. P. Huang, *Int. J. Hydrogen Energy*, 2017, **42**, 23578–23586.
39 Z. Wei, Y. Lu, J. Zhao, S. Zhao, R. Wang, N. Fu, X. Li, L. Guan and F. Teng, *ACS Omega*, 2018, **3**, 137–143.
40 X. Zheng, F. Kang, C. Huang, S. Lv and J. Zhang, *J. Ind. Eng. Chem.*, 2020, **88**, 186–195.
41 G. Greczynski and L. Hultman, *Prog. Mater. Sci.*, 2020, **107**, 100591.
42 H. T. Vu, G. T. T. Pham, T. L. H. Doan, T. D. Lam, N. T. Van, N. V. Manh, P. T. Quyen, N. D. Hai, H. V. Doan and M. B. Nguyen, *J. Taiwan Inst. Chem. Eng.*, 2024, **161**, 105518.
43 B. Deng, Y. Zhu, J. Li, X. Chen, K. He, J. Yang, K. Qin, Z. Bi, X. Xiao, S. Chen, X. Xu and G. Xu, *J. Alloys Compd.*, 2021, **851**, 155439.
44 V. Poliukhova, S. Khan, Z. Qiaohong, J. Zhang and D. Kim, *Appl. Surf. Sci.*, 2022, **575**, 151773.
45 M. B. Nguyen, G. H. Le, T. Duy, Q. K. Nguyen, T. Trang, T. Pham, T. Lee and T. A. Vu, *J. Hazard. Mater.*, 2021, **420**, 126560.
46 S. Nor, Q. Aini, A. Aziz, K. Chee, S. Pung, Z. Lockman, A. Ulhamid and W. Kian, *J. Ind. Eng. Chem.*, 2023, **118**, 226–238.
47 H. V. T. Nguyen, M. B. Nguyen, H. V. Doan and X. N. Pham, *Mater. Res. Express*, 2023, **10**(8), 085506.
48 P. Huang, G. Yuan, T. Wei, J. Li and M. N. R. Ashfold, *RSC Adv.*, 2018, **8**, 20686–20691.
49 H. Ren, L. Ge, Q. Guo, L. Li, G. Hu and J. Li, *RSC Adv.*, 2018, **8**, 20157–20165.
50 A. Raja, N. Son, M. Swaminathan and M. Kang, *J. Colloid Interface Sci.*, 2021, **602**, 669–679.
51 Q. Cui, X. Gu, Y. Zhao, K. Qi and Y. Yan, *J. Taiwan Inst. Chem. Eng.*, 2023, **142**, 104679.
52 M. D. Donohue and G. L. Aranovich, *Adv. Colloid Interface Sci.*, 1998, **76–77**, 137–152.
53 M. Han, Z. Wang, Z. Zhang, S. Wang, G. Wang, K. Hou, H. Zhang, L. Jiang and G. Hu, *Chem. Eng. Sci.*, 2023, **281**, 119151.
54 R. Boulkroune, M. Sebais, Y. Messai, R. Bourzami, M. Schmutz, C. Blanck, O. Halimi and B. Boudine, *Bull. Mater. Sci.*, 2019, **42**, 1–8.

55 S. Aslam, F. Mustafa, M. A. Ahmad, M. Saleem, M. Idrees and A. S. Bhatti, *Ceram. Int.*, 2018, **44**, 402–408.
56 S. Zhang, X. Tang, L. Zang and L. Zhao, *Talanta*, 2024, **272**, 125811.
57 X. N. Pham, H. T. Nguyen, T. N. Pham, T. T. B. Nguyen, M. B. Nguyen, V. T. T. Tran and H. V. Doan, *J. Taiwan Inst. Chem. Eng.*, 2020, **114**, 91–102.
58 R. Acharya and K. Parida, *J. Environ. Chem. Eng.*, 2020, **8**, 103896.